

# Direct visualization of orbital electron occupancy

**Tongtong Shang**

Institute of Physics, Chinese Academy of Sciences

**Dongdong Xiao**

Institute of Physics, Chinese Academy of Sciences

**Fanqi Meng**

Tsinghua University

**Xiaohui Rong**

Institute of Physics, Chinese Academy of Sciences

**Xiaozhi Liu**

Institute of Physics <https://orcid.org/0000-0001-8647-8694>

**Xinyan Li**

Institute of Physics, Chinese Academy of Sciences

**Qinghua Zhang**

Institute of Physics

**Yuren Wen**

University of Science and Technology Beijing

**Xuefeng Wang**

Institute of Physics, Chinese Academy of Sciences

**Dong Su**

Institute of Physics, Chinese Academy of Sciences <https://orcid.org/0000-0002-1921-6683>

**Yong-Sheng Hu**

Institute of Physics, Chinese Academy of Sciences

**Hong Li**

Institute of Physics <https://orcid.org/0000-0002-8659-086X>

**Qian Yu**

Zhejiang University

**Ze Zhang**

Zhejiang University

**Vaclav Petricek**

The Academy of Sciences of the Czech Republic <https://orcid.org/0000-0002-9731-8730>

**Lijun Wu**

Brookhaven National Laboratory <https://orcid.org/0000-0002-8443-250X>

**Lin Gu** (✉ [l.gu@iphy.ac.cn](mailto:l.gu@iphy.ac.cn))

Beijing National Laboratory for Condensed Matter Physics, Institute of Physics, Chinese Academy of Sciences, Beijing 100190, China <https://orcid.org/0000-0002-7504-031X>

**Jian-Min Zuo**

University of Illinois, Urbana-Champaign

**Yimei Zhu**

Brookhaven National Laboratory

**Ce Wen Nan**

Tsinghua University <https://orcid.org/0000-0002-3261-4053>

**Jing Zhu**

Tsinghua University

---

## Article

**Keywords:** orbital occupancy, valence electron distribution, quantitative convergent-beam electron diffraction, synchrotron powder X-ray diffraction

**Posted Date:** May 25th, 2021

**DOI:** <https://doi.org/10.21203/rs.3.rs-499157/v1>

**License:**  This work is licensed under a Creative Commons Attribution 4.0 International License.  
[Read Full License](#)

---

## Direct visualization of orbital electron occupancy

Tongtong Shang<sup>1,2†</sup>, Dongdong Xiao<sup>1,3†</sup>, Fanqi Meng<sup>4†</sup>, Xiaohui Rong<sup>1</sup>, Xiaozhi Liu<sup>1,2</sup>, Xinyan Li<sup>1,2</sup>, Qinghua Zhang<sup>1</sup>, Yuren Wen<sup>5</sup>, Xuefeng Wang<sup>1,2</sup>, Dong Su<sup>1,2</sup>, Yong-sheng Hu<sup>1,2</sup>, Hong Li<sup>1,2</sup>, Qian Yu<sup>6</sup>, Ze Zhang<sup>6</sup>, Vaclav Petricek<sup>7</sup>, Lijun Wu<sup>8\*</sup>, Lin Gu<sup>1,2,3\*</sup>, Jian-Min Zuo<sup>9</sup>, Yimei Zhu<sup>8</sup>, Ce-Wen Nan<sup>4</sup>, Jing Zhu<sup>10</sup>

### Affiliations:

<sup>1</sup>Beijing National Laboratory for Condensed Matter Physics, Institute of Physics, Chinese Academy of Sciences, Beijing 100190, P. R. China

<sup>2</sup>School of Physical Sciences, University of Chinese Academy of Sciences, Beijing 100049, China

<sup>3</sup>Songshan Lake Materials Laboratory, Dongguan, Guangdong 523808, P. R. China

<sup>4</sup>State Key Lab of New Ceramics and Fine Processing, School of Materials Science and Engineering, Tsinghua University, 100084 Beijing, P. R. China

<sup>5</sup>School of Materials Science and Engineering, University of Science and Technology Beijing, Beijing 100083, P. R. China

<sup>6</sup>Department of Materials Science and Engineering, Center of Electron Microscopy and State Key Laboratory of Silicon Materials, Zhejiang University, 310027, Hangzhou, P. R. China

<sup>7</sup>Institute of Physics, Academy of Sciences of the Czech Republic, 2, 180 40 Praha 8, Czech Republic

<sup>8</sup>Condensed Matter Physics and Materials Science Division, Brookhaven National Laboratory, Upton, New York 11973, USA

<sup>9</sup>Department of Materials Science and Engineering, University of Illinois at Urbana Champaign, 1304 W Green St, Urbana, IL 61801, USA

<sup>10</sup>Beijing National Center for Electron Microscopy, Laboratory of Advanced Materials, Department of Materials Science and Engineering, Tsinghua University, Beijing 100084, P. R. China

\*Email: [ljwu@bnl.gov](mailto:ljwu@bnl.gov); [l.gu@iphy.ac.cn](mailto:l.gu@iphy.ac.cn)

### Abstract

Orbital is one of the primary physical parameters that determine materials' properties. Currently, experimentally revealing the electron occupancies of orbitals under the control of external field remains a big challenge due to the stringent requirements for samples such as the atomically sharp surface or defect-free large-size single crystals. Here, we developed a method with the combination of quantitative convergent-beam electron diffraction and synchrotron powder X-ray diffraction, and

demonstrated the visualization of the real-space orbital occupancy by choosing LiCoO<sub>2</sub> as a prototype. Through multipole modelling of the accurately measured structure factors, we found the opposite changes of Co  $t_{2g}$  and  $e_g$  orbital occupancies under different electrochemical states which can be well-correlated with the CoO<sub>6</sub> octahedra distortion. This robust method provides a feasible route to quantify the real-space orbital occupancy on small-sized particles, and opens up a new avenue for exploring the orbital origin of physical properties for functional materials.

**Keywords:** orbital occupancy, valence electron distribution, quantitative convergent-beam electron diffraction, synchrotron powder X-ray diffraction

Materials' properties are usually tuned by physical parameters including lattice, charge, orbital and spin<sup>1, 2</sup>. The lattice composed of the periodic arrangement of atoms is the structural basis to understand the physical properties of materials. The electrons have three attributes including charge, spin, and orbital, which give rise to a wide range of functional properties of materials such as electrical, magnetic, optical, and thermal properties along with the underlying crystal lattice<sup>3, 4</sup>. Understanding the origin of these distinctive functionalities in materials therefore critically relies on our ability to accurately measure both electron's degrees of freedom and lattice for revealing their complex interactions. Over the years, the remarkable progress in the microscopy, spectroscopy and diffraction has enabled to probe the lattice, charge and spin with high precision and sensitivity, which has made significant contributions to reveal fundamental physical mechanisms for the relevant functional properties that have made up the cornerstone of current electric devices (such as field-effect transistors, magnetic random-access memory and piezoelectric transducers)<sup>5-9</sup>. By contrast, much less advancement has been made on the detection and characterization of electron orbital on a specific atom in the materials. Although it is well known that orbital degree of freedom plays an important role in many novel physical phenomena (e.g., high temperature superconductivity, colossal magnetoresistance, metal-insulator transition, and topological states of matter as well as in (electro)chemistry<sup>10-12</sup>. Revealing the underlying real-space orbital physics will not only deepen our understanding on the emergent functionalities of materials and (electro)chemical processes, but also provide a new knob to tune the properties of functional materials.

Theoretically, density functional theory (DFT) has been developed to reveal the ground-state electron density and successfully explains the origin of the unique functionalities and predicts new properties for various materials<sup>13</sup>. Although great advance has been made on quantifying bonding interactions and electronic structures, it is limited by the computer processing power which can only calculate several unit cells at ground-state and may miss some chemical interactions under the external field in practice<sup>14, 15</sup>. Over the past decades, improvements of methodology have made it possible to measure the charge density of materials. Although the orbital sensitivity of scanning tunneling microscopy (STM) with a well-controlled calibration of tip-sample distance has been demonstrated<sup>16, 17</sup>, it can only visualize orbital relying on the freshly cleaved and atomically sharp

surfaces under the ultra-high vacuum environment<sup>18</sup>. Thus, there are serious limitations in applications. Because the electron orbital represents the shape of the electron cloud in a solid, the most intuitive way to resolve the orbital configuration is to accurately measure the electron density distribution around the bonding atoms, which are coded in the structure factors through Fourier transformation. Compared with other methods which can be employed for structure-factor measurement, single-crystal X-ray diffraction (SCXRD) is the primary approach. Unfortunately, it suffers from defects, extinction effect, and absorption that degrade the measurement accuracy for low-order structure factors which carry most information of the valence electron density, especially for functional materials containing heavy elements<sup>19</sup>. Instead, electron diffraction is extinction-free and more sensitive at low scattering angles compared with XRD, which makes it more suitable for low-order reflections<sup>20, 21</sup>. Besides, quantitative convergent-beam electron diffraction (QCBED) with nanometer-sized electron beam can be used to obtain structure factors from perfect crystal regions so that the dynamic diffraction theory for perfect crystal can be applied. Based on the many-beam dynamic diffraction theory, the intensity distribution of CBED patterns can be obtained through solving the Schrödinger equation under the periodic potential field in crystals, which is compared to experimental patterns to get low-order structure factors<sup>22-25</sup>. In addition, low temperature (100 K), short-wavelength (0.41343 Å) and high resolution ( $\sin\theta/\lambda_{\max} \geq 1.2 \text{ \AA}^{-1}$ ) synchrotron powder X-ray diffraction (SPXRD) with negligible absorption effect can accurately measure the high-order structure factors and Debye-Waller factors of small-sized particles which are not accessible by SCXRD. Moreover, the acquisition of electron diffraction and SPXRD at the same temperature ensures that the thermal vibrations are the same, making the experimental results more accurate and precise. However, to the best of our knowledge, the combination of QCBED and SPXRD has not been realized. What is more, the quantitative topological analysis of the refined electron density based on the results from QCBED has also not been performed. Combing the strengths of QCBED and SPXRD, it becomes possible to accurately measure the shape of the valence electron clouds around bonding atoms and quantify the orbital occupancy to uncover the origin of properties for functional materials beyond the scope of the crystal lattice and charge under the control of external fields.

Here, we use LiCoO<sub>2</sub> as a model material and apply the method described above to successfully

resolve a mystery in its electrochemical properties from the orbital point-of-view. As is well-known, LiCoO<sub>2</sub> is the first cathode material used for commercial LIBs and still dominates in the portable electronics market because of many unique advantages including high electron conductivity, high volumetric energy density as well as excellent cycle life<sup>26</sup>. However, only limited voltage can be applied to extract no more than 60% Li to maintain a reasonable cycle-reversibility. Much work focused on the charge compensation mechanism of LiCoO<sub>2</sub> during electrochemical charging and found that oxygen is involved in the redox reaction in highly charged LiCoO<sub>2</sub><sup>27</sup>. In addition, there have been many effective strategies to improve the cycle stability of LiCoO<sub>2</sub> at high voltage<sup>28-30</sup>. However, the relationship between the lattice and the electronic structure in detail remains ambiguous. Here, we choose Li<sub>1-x</sub>CoO<sub>2</sub> with four different states of charge (SOC) ( $x=0, 0.4, 0.6, 0.7$ ) to map the valence electron distribution of Co and O atoms by combining of QCBED with high energy SPXRD. With the new knowledge, we find the relationships between the crystal structure, the charge and the orbitals of LiCoO<sub>2</sub> during charging, and explore its electrochemical properties from the orbital point-of-view, by measuring the aspherical distribution of electron density and establishing the relations between the occupancies of Co *d*-orbitals and the populations of multipole density functions.

The electron density of Li<sub>1-x</sub>CoO<sub>2</sub> was determined using the multipole modelling of the experimental structure factors<sup>31</sup> with a resolution of  $\sin \theta / \lambda \geq 1.2 \text{\AA}^{-1}$  that insures sufficiently high resolution and precision. **Fig. 1** is the schematic of the whole procedure showing how one can accurately obtain the electron density distribution in a crystal material and distinguish the changes of the orbital occupancies for transition-metal ions under the ligand field in polyhedrons by combining QCBED with high-energy SPXRD techniques. The crystal structure parameters of Li<sub>1-x</sub>CoO<sub>2</sub> including lattice constants, atomic positions and Debye-Waller factors, and high-order structures can be accurately extracted from SPXRD through Rietveld refinement. In order to reduce systematic errors, low temperature (100K) was used for all data collection to minimize the thermal diffuse scattering and anharmonicity that contributes to the background and high-order Bragg reflections, and finally to enhance the signal-to noise ratio of diffraction data<sup>32</sup>. The low-order structure factors were accurately measured by QCBED at 100K to ensure that the X-ray and electron measurements were done at almost the same temperature. In the meantime, low-temperature measurements can

reduce the beam damage during CBED acquisition. The initial structure parameters obtained by Rietveld refinement from SPXRD are employed for Bloch wave calculation, during which the thickness, beam direction and structure factors are treated as refinable parameters. The refinement was made by comparing the experimental intensity profile across CBED systematic rows with the calculated intensity using a goodness of fit criterion<sup>20</sup>. It is worth noting that these experimental structure factors are model independent<sup>33</sup>. **Fig. 2** displays the five low-order structure factors measurements including (003), (0̄11), (006), (012), and (0̄14) for LiCoO<sub>2</sub>, where good agreement between the experimental intensity and the calculated one is reached. All refined low-order structure factors at different SOC are listed in **Table S1-S4**.

Atom-centered multipole expansion<sup>19</sup>, which is based on the spherical harmonic functions, has been proven to be successful to describe the real space non-spherical electron density, in which the electron density of each atoms is described as:

$$\rho(\mathbf{r}) = \rho_c + P_v \kappa^3 \rho_v(\kappa r) + \sum_{l=0}^{l_{max}} \kappa'^3 R_l(\kappa' r) \sum_{m=0}^l P_{lm\pm} d_{lm\pm}(\theta, \phi) \quad (1)$$

where  $\rho_c$  and  $\rho_v$  are the core and valence electron densities, respectively.  $P_v$  and  $P_{lm\pm}$  are the population parameters of valence electron density and spherical harmonic density  $d_{lm\pm}$ , respectively.  $\kappa$  and  $\kappa'$  are valence-shell contraction-expansion parameters.  $R_l$  is the radial function. This method implicitly assigns each density fragment to the centered nucleus. Therefore, the shape of the observed electron density can be flexibly fitted by a sum of non-spherical pseudo-atomic densities. These consist of a spherical-atom (or ion) electron density obtained from multi-configuration Dirac-Fock calculations with variable orbital occupation factors to allow for charge transfer, and a small non-spherical part in which local symmetry-adapted spherical harmonic functions were used<sup>20</sup>.

Bader's quantum theory of atoms in molecules (QTAIM) and deformation densities often used to analyze the charge transfer and chemical bonding interactions in crystals after obtaining the real-space electron density distribution<sup>34, 35</sup>. QTAIM can provide a unique definition of bonding interactions by using the bond critical point (BCP). The BCP is defined as a critical point in the electron density, where a maximum in two directions (perpendicular to the bond), and a minimum in one direction (parallel to the bond) occur. In order to quantitatively evaluate the Co-O bonding interactions of Li<sub>1-x</sub>CoO<sub>2</sub> during charging, the Bader's topological analysis was performed based on

the multipole modeling electron density<sup>31</sup>. The electron density topological analysis on BCPs illustrated in **Table 1**, indicates that the Co-O interaction is the closed-shell interaction<sup>36</sup> in the whole charging process, with the positive  $\nabla^2\rho(r_c)$  and  $|\lambda_1|/\lambda_3 \ll 1$ . But the relatively large  $\rho(r_c)$  suggests the covalent component in  $\text{Li}_{1-x}\text{CoO}_2$  and, hence, the Co-O bond is partially covalent. This may be caused by the high electron density at the positions of the Co nuclei, which results in a sharp decrease along the Co-O bond path and large curvature  $\lambda_3$  at the BCP<sup>37</sup>.

Deformation densities, which is the difference between the refined multipole electron density and the reference model from the superposition of spherical isolated-atoms, show an intuitive charge accumulation and depletion in chemical bonding regions as well as deformation around transition metals in line with *d*-orbital energy splitting under the ligand field<sup>35</sup>. **Fig. 3** exhibits the static deformation density in the  $(01\bar{4})$  plane which contains a  $\text{CoO}_4$  plane of the  $\text{CoO}_6$  octahedra. In **Fig. 3B** the shape of Co  $e_g$  and  $t_{2g}$  and O  $2p$  orbitals under the metal-ligand interaction can be clearly seen. The electron accumulation region surrounding the Co nuclei colored by red corresponds to the  $d_{xy}$  orbital with lower energy compared to the  $d_{x^2-y^2}$  orbital (blue region). This deformation density shows that the valence electrons occupy the  $t_{2g}$  orbital rather than the  $e_g$  orbital of the Co atom in the  $\text{CoO}_6$  octahedra, which agrees with the  $3d$ -orbital populations of Co as seen in **Table 2**. However, with decreasing Li content, the accumulation and depletion of the valence electron density in terms of the  $t_{2g}$  and  $e_g$  orbital, respectively, becomes more and more inapparent as seen from **Fig. 3B** to **Fig. 3E**. This change indicates the difference between the  $t_{2g}$  and  $e_g$  orbital population is getting smaller. With the extraction of lithium ions, a Mott insulator-metal transition will happen when  $x > 0.25$ <sup>38</sup>. The continually introducing of lithium vacancies accompanied with the rehybridization of Co and O, may leads to the hole character on O  $2p$  orbital and Co  $t_{2g}$  orbital, and electron accumulation in the Co  $e_g$  orbital. These above variations give rise to the disappearance of the features surrounding the Co and O nucleus as seen in **Fig. 3B**.

Because it is difficult to clarify the evolution of Co-O interactions in the  $\text{CoO}_6$  octahedra in terms of the features at BCPs along the Co-O bond and deformation density around Co atom, we list the refined Co  $3d$  and O  $2p$  valence electron populations to quantitatively analyze the variation trend during electrochemical charging. From  $x=0$  to  $x=0.4$ , the number of refined valence electrons of Co and O decreased. This indicates the oxidation of Co and the enhanced covalency of Co and O

at the initial stage of the charging process. With the Li contents further decreasing, the refined valence electron of Co increases and vice versa for O. This suggested that oxygen was oxidized at relatively highly charged state for  $\text{LiCoO}_2$ . To further quantify the evolution of Co  $3d$ -orbital population and reveal the relationship of the lattice structure and the orbital, Co  $3d$ -orbital occupancies under different SOC were calculated from the refined multipole population parameters. Since the  $3d$ -orbital electrons can be described in terms of atomic orbitals<sup>39</sup>  $d_i$ :

$$\rho_{3d} = \sum_{i=1}^5 P_i d_i^2 + \sum_{i=1}^5 \sum_{j>i}^5 P_{ij} d_i d_j \quad (2)$$

where  $d_i = R(r)y_{lm\pm}$ ,  $R(r)$  is the radial function,  $y_{lm\pm}$  is the spherical harmonic function and  $P$  is the population parameter of atomic orbital. This expression equals to the valence part of **Eq.1**. Thus, the relationship between  $d$ -orbital occupancies and multipole population parameters is casted in the form of a  $15 \times 15$  matrix, and reduce to smaller size under different site symmetries<sup>39</sup>. In  $\text{LiCoO}_2$ , the site symmetry of Co is  $\bar{3}m$  with a  $4 \times 4$  matrix which converts the multipole populations to the  $e_g$  and  $t_{2g}$  orbital occupancies<sup>40</sup>, as shown in **Table 2**. Different from the principle that the higher energy  $e_g$  orbital should have zero population of Co ions in a fully ionic bond according to the ligand field theory, the experimental population of  $e_g$  orbital in pristine  $\text{LiCoO}_2$  is not zero and continuously increasing during charging. This indicates that the Co-O bond has covalent component in pristine  $\text{LiCoO}_2$ , where electrons from the O ions are partly shared with the Co ions<sup>15</sup>. The continuous extraction of Li ions leads to the hole density congregation in the Co  $t_{2g}$  orbital and rehybridization of the Co  $e_g$  and O  $2p$  orbitals. It is the increase of electrons in Co  $e_g$  orbitals and holes in O  $2p$  orbitals which results in the insulator to metal transition of  $\text{Li}_{1-x}\text{CoO}_2$ . What's more, the orbital rehybridization is related to the distortion of  $\text{CoO}_6$  octahedra (**Table S5**). The bond angle of O-Co-O in  $\text{CoO}_4$  plane is  $85.89^\circ$  in pristine  $\text{LiCoO}_2$  that deviate from the regular octahedra acting as the precondition. The anisotropic lattice constant variation caused by delithiation further increases the distortion of the  $\text{CoO}_6$  octahedron. As a result, the smaller bond angle and shorter bond length of Co-O bond is beneficial for the charge transfer from O  $2p$  to Co  $3d e_g$  orbital. Especially when  $x \geq 0.6$ , the total valence electrons of Co increase and that of O decrease, in line with the dramatic changes of lattice and electronic structure of the  $\text{CoO}_6$  framework (**Table 2** and **Table S5**). These variations aggravate the structure degradation and lead to the irreversible capacity fading of  $\text{LiCoO}_2$  at high voltage.

In summary, valence electron density distributions and  $3d$ -orbital occupancies of the Co atom in  $\text{Li}_{1-x}\text{CoO}_2$  have been quantitatively investigated based on modelling of highly accurate structure factors obtained by combining QCBED and SPXRD. The deformation density maps show the different variation trends of Co  $t_{2g}$  and  $e_g$  orbital populations in the  $\text{CoO}_6$  octahedra. Quantitative analysis of Co  $3d$ -orbital occupancies demonstrated that it is the decrease of  $t_{2g}$  electrons and the increase of  $e_g$  electrons during charging result in the continuous distortion of Co-O octahedron, and influence the structural stability of  $\text{LiCoO}_2$  in service. From the above findings, it is realized that the correlations between the lattice structure, the charge and the orbital of electrode materials are quite complicated. The polyhedron distortion is always accompanied by the changes of electron distribution and orbital configuration. The realization of the real-space orbital occupancy measurement makes it possible to reveal the direct correlations of lattice, charge and the orbital, shedding light on deep understanding of the intriguing physical properties such as orbital-mediated quantum phenomena, nontrivial strongly-correlated and topological systems.

### Acknowledgements

This work was supported by the Beijing Natural Science Foundation (No. Z190010), the National Key R&D Program of China (No. 2019YFA0308500), the Strategic Priority Research Program of Chinese Academy of Sciences (No. XDB07030200), the National Natural Science Foundation of China (No. 51421002, 51672307, 51991344, 52025025) and the Basic Science Centre Program of NSFC (No. 51788104).

### Author contributions

L.G. and L.J.W. planned and supervised the project. T.T.S. and D.D.X. designed research and analyzed CBED and XRD data with L.J.W., V.P., J.M.Z., and Y.M.Z.. X.H.R. prepared and electrochemically tested the samples. F.Q.M., X.Z.L. and X.Y.L. prepared the TEM samples. Q.H.Z. and Y.R.W. conducted the STEM measurement and analyzed data with X.F.W., D.S., Y-S.H., H.L., Q.Y., Z.Z. C-W. N. and J.Z.. T.T.S., D.D.X., F.Q.M., Q.Y., L.J.W. and L.G. wrote the manuscript with the help of other authors and all authors revised the manuscript.

### Competing interests

The authors declare no competing interests.

## Methods

**Sample preparation.** Pristine polycrystalline LiCoO<sub>2</sub> powder was bought from Alfa with a purity of 99.5%.

The delithiated samples were prepared using the electrochemical method. The high-loading electrodes (LiCoO<sub>2</sub> loading mass ~100 mg) were charged/discharged to different states of charge in a Swagelok cell, with Li metal as the counter electrode (1M LiPF<sub>6</sub> in ethylene, dimethyl carbonate). Subsequently, the charged Swagelok cells were disassembled, and the obtained powder samples were washed three times with dimethyl carbonate before drying. The cell assembling/disassembling and powder washing/drying were carried out in an argon-filled glove-box.

The TEM samples were fabricated using focus ion beam (FIB) milling, FEI Helios 600i. To prevent surface damage from ion milling, a 40 nm thick carbon layer was deposited using thermal evaporation. On the top of the particle, a regular Pt protection layer was deposited with standard settings using an electron-beam at 5 kV, 86 pA for 300 nm thickness following by an ion-beam at 30 kV, 80 pA for 1 um thickness. The key point was to find a particle with a diameter of 4-6 um from hundreds of particles dispersed on a Si chip, and the Pt protection layer needs to be exactly perpendicular to the in-plane orientation of [100] and [110]. The particle was then directly lifted using nanomanipulator to a TEM grid. The thinning process was first performed using the FIB cleaning cross-section method (30 kV 0.79 nA, tilt ± 2°) until the lamella thickness reached 600 nm. Further fine milling reduced the lamella thickness to 100 nm (30 kV 80 pA) and the final polishing process was repeated by FIB at low voltage and low current (8 kV, 23 pA) until the lamella was about 35-50 nm thick. The final polishing step was conducted carefully to avoid lamella bending. To reduce the surface damage and the thickness of amorphous, low-energy focused Ar ion milling was conducted using Fischione 1040 NanoMill system.

**QCBED collection.** The CBED experiments were carried out using an aberration-corrected microscope, JEOL JEM-ARM200CF, equipped with a Gatan imaging filter and a 2048×2048 pixels 965 CCD camera. An energy window of 10 eV around the zero-loss energy was selected. Because

the energy filter was used in the QCBED experiment, inelastically scattered electrons were not included in the Bloch-wave calculations. The acceleration voltage was 197.50 kV, which was obtained by fitting the kinetically simulated CBED pattern to the experimental pattern taken from a single crystal sample of silicon.

**SPXRD measurements.** Polycrystalline samples of  $\text{Li}_{1-x}\text{CoO}_2$  were sealed in a 0.3 mm internal diameter Lindeman glass capillary. Synchrotron powder X-ray profiles were measured at the SPring-8 BL19B2 beamline. A large Debye-Sherrer camera with an imaging plate (IP) detector was used for data collection. The data were collected at 100 K using a  $\text{N}_2$  gas flow low temperature device. The wavelength of the incident X-rays was 0.413269 Å by calibration with a NIST  $\text{CeO}_2$  standard sample. Data were collected to  $\sin\theta/\lambda_{\max}=1.67 \text{ \AA}^{-1}$ .

**STEM characterization.** STEM images and acquisitions were performed on a probe-aberration-corrected microscope, JEOL JEM-ARM200CF, at 200 kV with a 25 *mrad* incident beam and a collection angle between 90 and 370 *mrad* for HAADF acquisition.

## Reference

1. Mannhart J, Schlom DG. Oxide Interfaces-An Opportunity for Electronics. *Science* 2010, **327**(5973): 1607-1611.
2. Hwang HY, Iwasa Y, Kawasaki M, Keimer B, Nagaosa N, Tokura Y. Emergent phenomena at oxide interfaces. *Nature Materials* 2012, **11**(2): 103-113.
3. Wang C, Zhang M, Chen X, Bertrand M, Shams-Ansari A, Chandrasekhar S, *et al.* Integrated lithium niobate electro-optic modulators operating at CMOS-compatible voltages. *Nature* 2018, **562**(7725): 101-104.
4. Hwang J, Feng Z, Charles N, Wang XR, Lee D, Stoerzinger KA, *et al.* Tuning perovskite oxides by strain: Electronic structure, properties, and functions in (electro)catalysis and ferroelectricity. *Materials Today* 2019, **31**: 100-118.
5. Nellist PD, Chisholm MF, Dellby N, Krivanek OL, Murfitt MF, Szilagyi ZS, *et al.* Direct Sub-Angstrom Imaging of a Crystal Lattice. *Science* 2004, **305**(5691): 1741.
6. MacLaren I, Ramasse QM. Aberration-corrected scanning transmission electron microscopy for atomic-resolution studies of functional oxides. *International Materials Reviews* 2014, **59**(3): 115-131.
7. Wu RJ, Udyavara S, Ma R, Wang Y, Chhowalla M, Birol T, *et al.* Visualizing the metal-MoS<sub>2</sub> contacts in two-dimensional field-effect transistors with atomic resolution. *Physical Review Materials* 2019, **3**(11): 111001.
8. Chen XZ, Feng JF, Wang ZC, Zhang J, Zhong XY, Song C, *et al.* Tunneling anisotropic magnetoresistance driven by magnetic phase transition. *Nature Communications* 2017, **8**(1): 449.
9. Choi KJ, Biegalski M, Li YL, Sharan A, Schubert J, Uecker R, *et al.* Enhancement of Ferroelectricity in Strained BaTiO<sub>3</sub> Thin Films. *Science* 2004, **306**(5698): 1005.
10. Shimojima T, Sakaguchi F, Ishizaka K, Ishida Y, Kiss T, Okawa M, *et al.* Orbital-Independent Superconducting Gaps in Iron Pnictides. *Science* 2011, **332**(6029): 564.
11. Kim H, Yoshida Y, Lee C-C, Chang T-R, Jeng H-T, Lin H, *et al.* Atomic-scale visualization of surface-assisted orbital order. *Science Advances* 2017, **3**(9).
12. Chakhalian J, Freeland JW, Habermeier HU, Cristiani G, Khaliullin G, van Veenendaal M, *et al.* Orbital Reconstruction and Covalent Bonding at an Oxide Interface. *Science* 2007, **318**(5853): 1114.
13. Zaanen J, Sawatzky GA, Allen JW. Band gaps and electronic structure of transition-metal compounds. *Physical Review Letters* 1985, **55**(4): 418-421.
14. Marianetti CA, Kotliar G, Ceder G. A first-order Mott transition in Li<sub>x</sub>CoO<sub>2</sub>. *Nature Materials* 2004, **3**(9): 627-631.
15. Kasai H, Tolborg K, Sist M, Zhang J, Hathwar VR, Filsø MØ, *et al.* X-ray electron density investigation of chemical bonding in van der Waals materials. *Nature Materials* 2018, **17**(3): 249-252.
16. Calleja F, Arnau A, Hinarejos JJ, Vázquez de Parga AL, Hofer WA, Echenique PM, *et al.* Contrast Reversal and Shape Changes of Atomic Adsorbates Measured with Scanning Tunneling Microscopy. *Physical Review Letters* 2004, **92**(20): 206101.
17. Woolcot T, Teobaldi G, Pang CL, Beglitis NS, Fisher AJ, Hofer WA, *et al.* Scanning Tunneling Microscopy Contrast Mechanisms for TiO<sub>2</sub>. *Physical Review Letters* 2012, **109**(15): 156105.
18. Yi M, Zhang Y, Shen Z-X, Lu D. Role of the orbital degree of freedom in iron-based

- superconductors. *npj Quantum Materials* 2017, **2**(1): 57.
- 19. Coppens P. *X-ray charge densities and chemical bonding*. Oxford University Press: International Union of Crystallography, 1997.
  - 20. Zuo JM, Kim M, O'Keeffe M, Spence JCH. Direct observation of d-orbital holes and Cu-Cu bonding in Cu<sub>2</sub>O. *Nature* 1999, **401**(6748): 49-52.
  - 21. Zheng JC, Zhu YM, Wu LJ, Davenport JW. On the sensitivity of electron and X-ray scattering factors to valence charge distributions. *Journal of Applied Crystallography* 2005, **38**: 648-656.
  - 22. Zhu J, Miao Y, Guo JT. The effect of boron on charge density distribution in Ni<sub>3</sub>Al. *Acta Materialia* 1997, **45**(5): 1989-1994.
  - 23. Spence JCH, Zuo JM. *Electron Microdiffraction*. Springer Science+Business Media: New York, 1992.
  - 24. Zuo JM. Quantitative convergent beam electron diffraction. *Materials Transactions Jim* 1998, **39**(9): 938-946.
  - 25. Jiang B, Zuo JM, Chen Q, Spence JCH. Orbital ordering in LaMnO<sub>3</sub>: estimates of structure factors and comparison of measurement methods. *Acta Crystallographica Section A* 2002, **58**: 4-11.
  - 26. Lyu Y, Wu X, Wang K, Feng Z, Cheng T, Liu Y, et al. An Overview on the Advances of LiCoO<sub>2</sub> Cathodes for Lithium-Ion Batteries. *Advanced Energy Materials* 2020, **n/a**(n/a): 2000982.
  - 27. Hu E, Li Q, Wang X, Meng F, Liu J, Zhang J-N, et al. Oxygen-redox reactions in LiCoO<sub>2</sub> cathode without O–O bonding during charge-discharge. *Joule* 2021.
  - 28. Ceder G, Chiang YM, Sadoway DR, Aydinol MK, Jang YI, Huang B. Identification of cathode materials for lithium batteries guided by first-principles calculations. *Nature* 1998, **392**(6677): 694-696.
  - 29. Zhang J-N, Li Q, Ouyang C, Yu X, Ge M, Huang X, et al. Trace doping of multiple elements enables stable battery cycling of LiCoO<sub>2</sub> at 4.6 V. *Nature Energy* 2019, **4**(7): 594-603.
  - 30. Huang Y, Zhu Y, Fu H, Ou M, Hu C, Yu S, et al. Mg-pillared LiCoO<sub>2</sub>: Towards Stable Cycling at 4.6 V. *Angewandte Chemie International Edition* 2020, **n/a**(n/a).
  - 31. Václav P, Michal D, Lukáš P. Crystallographic Computing System JANA2006: General features. *Zeitschrift für Kristallographie - Crystalline Materials* 2014, **229**(5): 345-352.
  - 32. Schmokel MS, Bjerg L, Larsen FK, Overgaard J, Cenedese S, Christensen M, et al. Comparative study of X-ray charge-density data on CoSb<sub>3</sub>. *Acta Crystallographica Section A* 2013, **69**(6): 570-582.
  - 33. Zhu Y, Zheng JC, Wu L, Frenkel AI, Hanson J, Northrup P, et al. Nanoscale disorder in CaCu<sub>3</sub>Ti<sub>4</sub>O<sub>12</sub>: A new route to the enhanced dielectric response. *Physical Review Letters* 2007, **99**(3).
  - 34. Bader RFW. Atoms in molecules. *Accounts of Chemical Research* 1985, **18**(1): 9-15.
  - 35. Tolborg K, Iversen BB. Electron Density Studies in Materials Research. *Chemistry – A European Journal* 2019, **0**(0).
  - 36. Gatti C. Chemical bonding in crystals: new directions. *Zeitschrift Fur Kristallographie* 2005, **220**(5-6): 399-457.
  - 37. Koritsanszky TS, Coppens P. Chemical Applications of X-ray Charge-Density Analysis. *Chemical Reviews* 2001, **101**(6): 1583-1628.
  - 38. Ménétrier M, Saadoune I, Levasseur S, Delmas C. The insulator-metal transition upon lithium deintercalation from LiCoO<sub>2</sub>: electronic properties and <sup>7</sup>Li NMR study. *Journal of Materials*

- Chemistry* 1999, **9**(5): 1135-1140.
39. Holladay A, Leung P, Coppens P. Generalized relations between d-orbital occupancies of transition-metal atoms and electron-density multipole population parameters from X-ray diffraction data. *Acta Crystallographica Section A* 1983, **39**(3): 377-387.
40. Stevens ED, Coppens P. Refinement of metal d-orbital occupancies from X-ray diffraction data. *Acta Crystallographica Section A* 1979, **35**(4): 536-539.

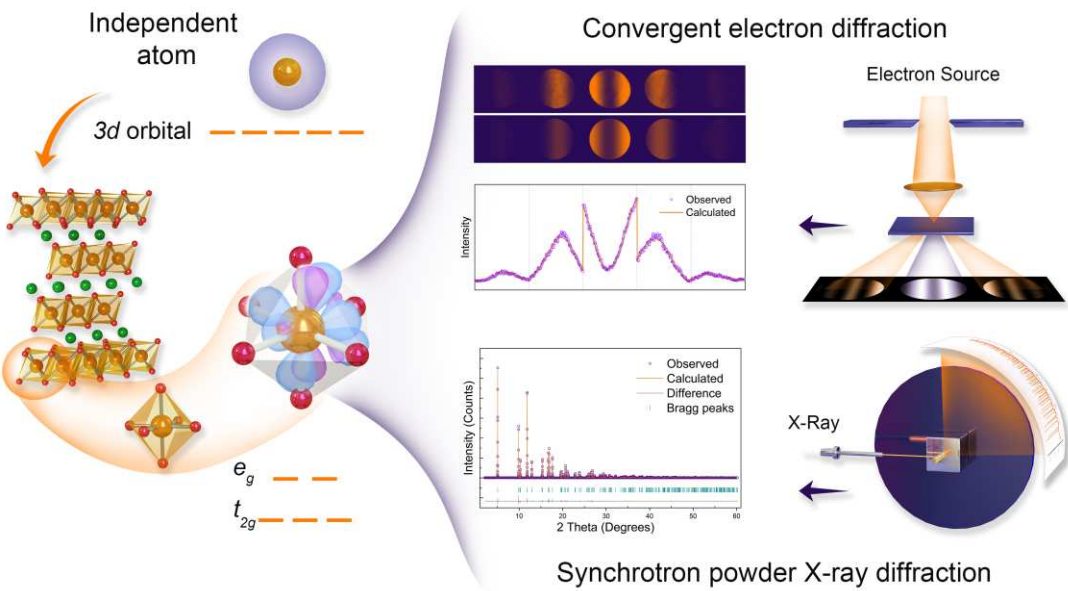


**Fig. 1. Experimental setup and the three-dimensional charge density in  $\text{LiCoO}_2$ .** The valence electron distribution of a free independent atom is spherical and the  $3d$ -orbitals energy are degenerated. In the case of crystals, the splitting of the energy level occurs under the ligand field in polyhedrons and the distribution of valence electrons changes which affected by the bonding interactions. This process produces abundant properties of functional materials. With the combination of QCBED and SPXRD, the deformed distribution of valence electron and orbital occupancies can be clearly detected. In terms of SPXRD, the structure information and high-order structure factors can be extracted through Rietveld refinement. For QCBED, low-order structure factors can be obtained using the Bloch wave method. Through multipole refinement and the quantitative topological analysis of the electron distribution, we can measure the occupancies of  $3d$  orbital.

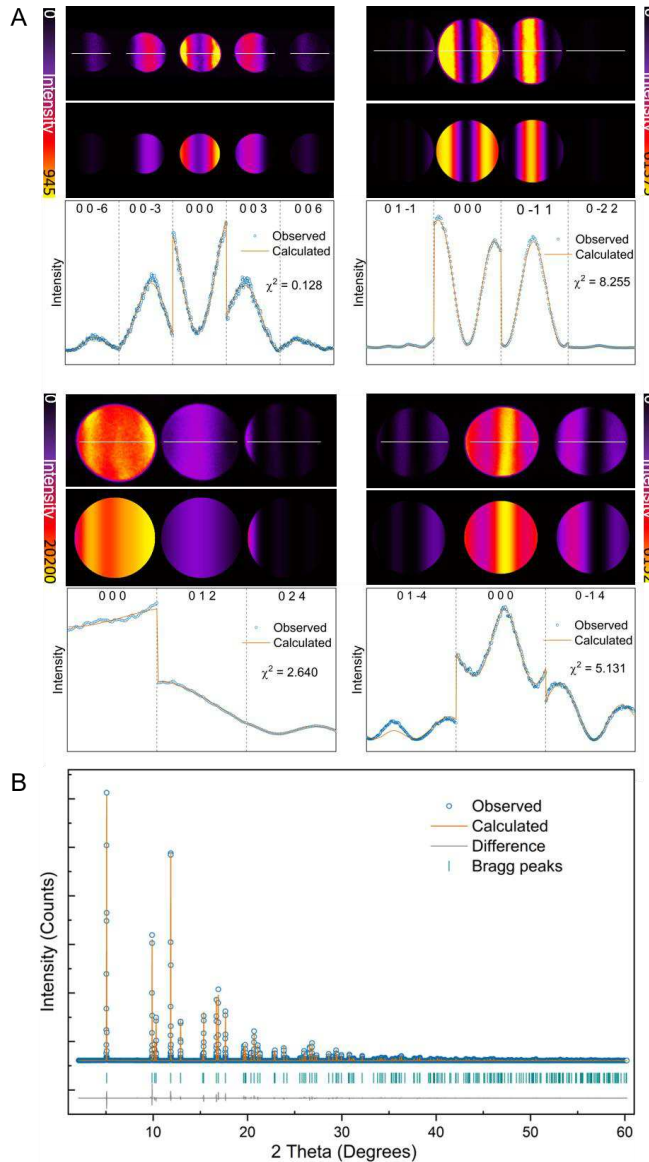


**Fig. 2. Extraction of structure factors.** (A) Examples the low-order electronic structure factors measurement for  $\text{LiCoO}_2$  (003), (006), (0 $\bar{1}$ 1), (012), and (0 $\bar{1}$ 4). The first row shows the energy-filtered CBED (003) systematic row pattern at 100K. The second row shows the calculated pattern based on the Bloch wave method corresponding to the experiments. Line scans of the intensity profile from the experimental pattern (dark cyan circle) and the calculated one (orange line) after the refinement are shown. (B) High-order X-ray structure factors measurement from the Rietveld refinement of SPXRD pattern of  $\text{LiCoO}_2$  (see Table S5 for details).

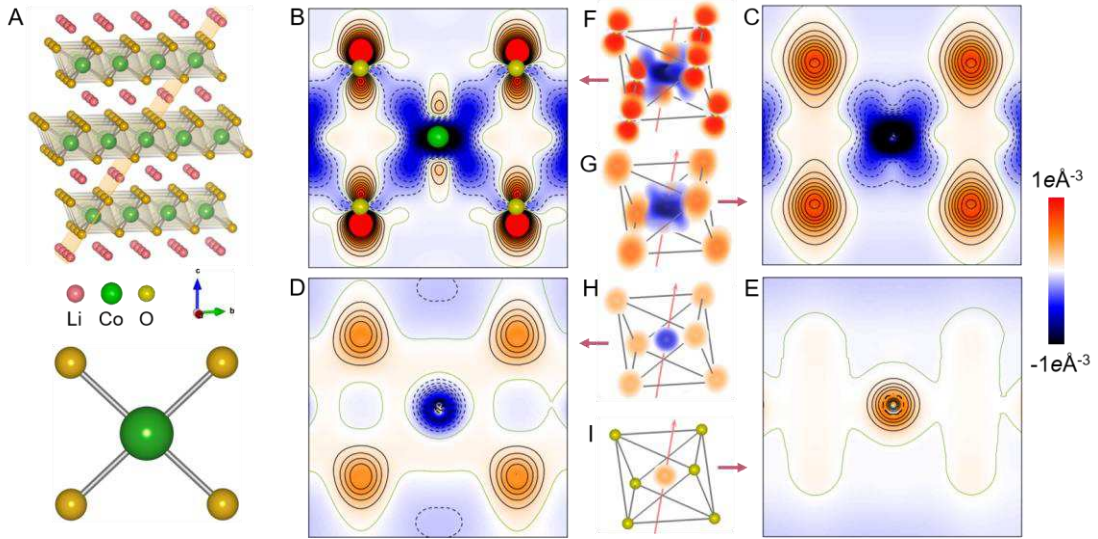


**Fig. 3. Charge density evolution for the Co-O and O-O interaction.** (A) At the top is the crystal structure of  $\text{LiCoO}_2$  with the indexed  $(01\bar{4})$  plane near the  $[100]$  direction. At the bottom is the  $(01\bar{4})$  plane that contains the  $\text{CoO}_4$  plane of the  $\text{CoO}_6$  octahedra. **B-E**, Static deformation density map of  $(01\bar{4})$   $\text{CoO}_4$  plane corresponding to the bottom  $\text{CoO}_4$  model of (A) with (B)  $\text{LiCoO}_2$ , (C)  $\text{Li}_{0.6}\text{CoO}_2$ , (D)  $\text{Li}_{0.4}\text{CoO}_2$  and (E)  $\text{Li}_{0.3}\text{CoO}_2$ . The charge density is shown in color using the color scheme on the right. All these maps use the same contour interval of  $0.1 \text{ e Å}^{-3}$ , with positive, negative and zero contours drawn as solid black, dash black and solid olive-green lines, respectively. **F-I**, 3D rendering of the static deformation density map of the  $\text{CoO}_6$  octahedra, viewed in the same direction as the top of (A) for (F)  $\text{LiCoO}_2$ , (G)  $\text{Li}_{0.6}\text{CoO}_2$ , (H)  $\text{Li}_{0.4}\text{CoO}_2$  and (I)  $\text{Li}_{0.3}\text{CoO}_2$  - see Fig. S3 for a clearer expression. The arrow points in the  $[001]$  direction. The same color scheme is used in the 3D view. For clarity, a translucency factor (alpha component in ARGB color) was used to remove the mostly white background.

**Table 1. Topological analysis of the bond critical points along Co-O bond in  $\text{Li}_{1-x}\text{CoO}_2$ .**

<b>Parameters</b>	<b><math>\text{LiCoO}_2</math></b>	<b><math>\text{Li}_{0.6}\text{CoO}_2</math></b>	<b><math>\text{Li}_{0.4}\text{CoO}_2</math></b>	<b><math>\text{Li}_{0.3}\text{CoO}_2</math></b>
$\rho$	0.5982	0.4732	0.6817	0.6151
$\nabla^2\rho$	10.49	15.79	13.43	15.43
$\nabla\rho$	$4.111 \times 10^{-6}$	$7.982 \times 10^{-6}$	$1.250 \times 10^{-6}$	$2.896 \times 10^{-6}$
$ \lambda_1 /\lambda_3$	0.17212	0.0602	0.2868	0.0732

$\rho$ ,  $\nabla\rho$  and  $\nabla^2\rho$  denote the electron density as well as its gradient and Laplacian, respectively. The Hess eigenvectors is defined by the diagonalization of the symmetric matrix of the nine second derivatives of  $\rho$ . Furthermore,  $\lambda_1$  and  $\lambda_3$  are the Hess eigenvalues perpendicular and parallel to the bond path at the critical point, respectively.

**Table 2.** The valence electron and calculated Co 3d-orbital populations from multipole parameters.

SOC	Co $\rho_{3d}$	Co $t_{2g}$	Co $e_g$	O $\rho_{2p}$
LiCoO <sub>2</sub>	6.50	4.83	1.67	6.75
Li <sub>0.6</sub> CoO <sub>2</sub>	6.44	4.19	2.25	6.58
Li <sub>0.4</sub> CoO <sub>2</sub>	6.66	4.26	2.40	6.37
Li <sub>0.3</sub> CoO <sub>2</sub>	7.24	2.81	4.43	6.03

## Supplementary Files

This is a list of supplementary files associated with this preprint. Click to download.

- [SupportingInformation.docx](#)